Correspondence to:

W. Fu and W.-L. Wang,
weiweif@uci.edu;
weilei.wang@xmu.edu.cn

Biogeochemical Equilibrium Responses to Maximal Productivity in High Nutrient Low Chlorophyll Regions

Weiwei Fu[1] and **Wei-Lei Wang[2]**

[1]Department of Earth System Science, University of California Irvine, Irvine, CA, USA, [2]State Key Laboratory of Marine Environmental Science, College of Ocean and Earth Sciences, Xiamen University, Xiamen, China

Abstract Whether ocean iron fertilization in high nutrient low chlorophyll (HNLC) regions is a practical geoengineering strategy to combat climate warming has been debated because the fate of absorbed carbon by the ocean remains unclear. We use an optimized oceanic biogeochemical inverse model to explore the equilibrium responses to increased productivity in major HNLC regions. We find an overall downward shift of nutrients and carbon from the surface and intermediate to the deep waters with maximal productivity in the HNLC Southern Ocean (SO), North Pacific (NP) and eastern equatorial Pacific (EP). The efficiency of soft tissue pump is increased by 37.8%, 2.7% and 5.4% in the SO, EP and NP simulation while atmospheric CO_2 concentration is drawn down by 45.1, 3.4 and 6.7 ppm, respectively. Meanwhile, global mean oxygen is decreased by 21.1%, 1.3% and 2.4% in the SO, EP and NP simulation, accompanied by an expansion of oxygen minimum zones by 400%, 26% and 63%, respectively. Our study indicates that iron fertilization has the potential to be an effective geoengineering approach to mitigate climate warming but has a strong impact on the development of ocean hypoxia.

Plain Language Summary Iron fertilization is proposed as a useful geoengineering tool to mitigate climate warming by stimulating phytoplankton growth and enhancing carbon export to deep ocean. However, the fate of the absorbed carbon in high nutrient low chlorophyll (HNLC) regions remains unclear. Here we use a data-constrained biogeochemical inverse model to explore the long-term impact of maximal productivity in different HNLC regions on ocean biogeochemistry and atmospheric CO_2. We performed a series of sensitivity tests that solved the new equilibrium states of key biogeochemical variables. Our results show that iron fertilization in all HNLC regions can reduce the atmosphere CO_2 by a maximum of 18.7%, demonstrating the usefulness of iron fertilization. However, iron fertilization also produces side effects including the loss of oxygen inventory and the production of powerful greenhouse gases, for example, N_2O. These side effects can offset the efficacy of iron fertilization and have detrimental impact on the ocean ecosystem.

1. Introduction

"High Nutrient Low Chlorophyll" (HNLC) conditions in the ocean refer to relatively low biomass of phytoplankton even with a plentiful supply of macronutrients (in particular, phosphate and nitrate). In the global ocean, there are three major high nutrient low chlorophyll (HNLC) regions, located in the subarctic North Pacific, the equatorial Pacific and the Southern Ocean. The three high nutrient low chlorophyll (HNLC) regions cover about 20% of the global ocean (Pitchford & Brindley, 1999). While the importance of the HNLCs is recognized for marine ecosystem and climate change, the cause of HNLCs has long been debated. Actively considered hypotheses include the scarcity of iron (Martin, 1990), top-down grazing control (Frost, 1991) and low light levels (Mitchell & Holmhansen, 1991). In particular, the hypothesis of iron limitation prompted a sequence of open ocean iron fertilization experiments in different HNLC regions (Boyd et al., 2007; Yoon et al., 2018).

Model experiments were conducted to investigate whether large-scale ocean iron fertilization (OIF) in the HNLC regions can be an effective means to sequester carbon from the atmosphere and slow down future climate warming (Joos, Siegenthaler, & Sarmiento, 1991; Sarmiento & Orr, 1991). In fact, such ocean iron fertilization (OIF) experiments did produce obvious biogeochemical responses such as increases in surface chlorophyll-*a*, drawdown of surface nutrients and reduction of surface pCO_2 (Boyd et al., 2007; Yoon et al., 2018). The increase of oceanic carbon uptake in model experiments with iron fertilization of hundreds of years was estimated to be 98–181 Pg C with models of different complexities (Joos, Sarmiento, & Siegenthaler, 1991; Kurz & Maier-reimer, 1993; Peng & Broecker, 1991; Sarmiento & Orr, 1991). Relatively, the HNLC in the Southern Ocean

is of particular importance because the Southern Ocean is characterized by deep water formation and carbon sink related to solubility change (Brown et al., 2019; Caldeira & Duffy, 2000; DeVries et al., 2017; Gruber et al., 2019; Landschutzer et al., 2014; Matear & Elliott, 2004; Rae et al., 2018). For example, iron supply in the Southern Ocean was shown as an important contributor to glacial-interglacial CO_2 change (Gaspari et al., 2006; Kohfeld et al., 2005; Watson et al., 2000). However, the long-term impact of productivity change induced by iron fertilization in HNLCs on ocean carbon uptake still remains unclear because it takes several thousand years for the ocean-atmosphere system to reach a new equilibrium level of CO_2. Thus, it is of critical importance to explore the equilibrium responses of the ocean to the changes of productivity in different HNLCs, caused by iron fertilization or other processes.

Past studies of iron fertilization experiments illustrated the great complexity of the ocean system (Blain et al., 2007; Street & Paytan, 2005; Strong et al., 2009). Attempts to engineer this system are likely to provoke complex, unpredictable responses. First, iron fertilization can increase productivity in an iron-fertilized area and reduce down-stream nutrients and phytoplankton biomass, leading to a spatial shift of biological productivity (Marinov et al., 2006; Moore et al., 2018; Primeau et al., 2013). Second, iron addition and subsequent phytoplankton blooms, associated with increased particulate organic matter export and remineralization, can reduce oxygen levels in subsurface waters (Keller et al., 2014; Oschlies et al., 2010). Therefore, there is a risk that the reduced oxygen level may result in increased production of nitrous oxide, a greenhouse gas far more powerful than CO_2 (Forster et al., 2007). However, the ultimate impact of these complex processes remains unclear.

In this study, we explore the impact of increased productivity in HNLCs with an optimized biogeochemical inverse model. Main objectives include: (a) to explore the equilibrium responses of global nutrients to elevated productivity in HNLC regions, (b) to evaluate the change of oxygen minimum zones (OMZs) and its impact on climate and (c) to quantify the impact of elevated productivity in different HNLC regions on atmospheric CO_2 in a coupled ocean-atmosphere system.

2. Methods

2.1. Biogeochemical Models

The inverse biogeochemical model includes three modules: phosphorus, carbon and oxygen module. The modeling method of the phosphorus module is the same as that in Wang et al. (2019). Briefly, we consider three pools of phosphorus: dissolved inorganic phosphorus (DIP), dissolved organic phosphorus (DOP) and particulate organic phosphorus (POP). The cycling of the three tracers is described using the following equations,

$$\left[\frac{d}{dt} + \mathbf{T}\right][\text{DIP}] = -\gamma[\text{DIP}] + \kappa_{dP}[\text{DOP}] + \kappa_g([\text{DIP}] - \overline{[\text{DIP}]}_{obs}$$

$$\left[\frac{d}{dt} + \mathbf{T}\right][\text{DOP}] = \sigma\gamma[\text{DIP}] + \kappa_P[\text{POP}] - \kappa_{dP}[\text{DOP}]$$

$$\left[\frac{d}{dt} + \mathbf{F}_{\text{POP}}\right][\text{POP}] = (1 - \sigma)\gamma[\text{DIP}] - \kappa_P[\text{POP}] \tag{1}$$

where $\mathbf{T}\left(\mathbf{T}[C] \equiv \nabla \cdot \left(\overrightarrow{U}[C] - \mathbf{K}\nabla[C]\right)\right)$ is an advection and diffusion transport operator that is used to model advection and diffusion transport of dissolved tracers. $\mathbf{T}$ is constrained using multiple tracers including temperature, salinity, sea surface height, CFC-11, CFC-12, ^{3}He, ^{14}C, and so on (Tim DeVries & Holzer, 2019). Particulate organic phosphorus (POP) sinks and gradually dissolves in the water column, its vertical distribution is modeled according to a power law function (a.k.a. Martin curve function), which is discretized to a sinking flux divergence operator ($\mathbf{F}_{\text{POP}}$). The exponent (b) is encoded in the $\mathbf{F}$ operator, and is optimized in the inversion. σ is a production allocation parameter that decides the fraction of production goes to dissolved organic phosphorus (DOP) and particulate organic phosphorus (POP), and is also optimized in the inversion. POP dissolution ($\kappa_P[\text{POP}]$) leads to the production of dissolved organic phosphorus (DOP), whose remineralization ($\kappa_{dP}[\text{DOP}]$) leads to the production of dissolved inorganic phosphorus (DIP). κ_g is a geological restoring parameter that is used to restore model dissolved inorganic phosphorus (DIP) concentration to the observed mean DIP concentration ($\overline{[\text{DIP}]}_{obs}$).

DIP assimilation rate ($\gamma(r)$) is modeled using satellite observed net primary production (NPP, SeaWiFS CbPM) and observed DIP concentration ($[\text{DIP}]_{obs}$) according to Equation 2.

$$\gamma(r) \equiv \begin{cases} \alpha \dfrac{\left[\dfrac{1}{r_{C:P}} \dfrac{\text{NPP}(r)}{\text{NPP}_0}\right]^{\beta}}{\dfrac{[\text{DIP}]_{\text{obs}}(r)}{[\text{DIP}]_0}}, & \textit{if } z < z_0, \\ \\ 0, & \textit{otherwise,} \end{cases} \qquad (2)$$

where α and β are free parameters that are optimized in the inversion. $r_{C:P}$ is a carbon to phosphorus ratio that is used to convert net primary production (NPP) from carbon unit to phosphorus unit. r represents location index. ~~net primary production~~ (NPP_0) and $[\text{DIP}]_0$ are set to 1 mmol C m^{-3} s^{-1} and 1 mmol m^{-3}, respectively, they are used to remove dimensions of $\text{NPP}(r)$ and $[\text{DIP}]_{\text{obs}}$. z_0 is the euphotic zone depth in the model, which is the top two model layers ($\sim$73 m).

The carbon model is more complicated compared to the phosphorus model, there are five explicit tracers: dissolved inorganic carbon (DIC), dissolved organic carbon (DOC), particulate organic carbon (POC), particulate inorganic carbon (PIC) as known as calcium carbonate, and total alkalinity (ALK). The governing equations are as follow,

right parenthesis is missing

$$\left[\frac{d}{dt} + \mathbf{T}\right][\text{DIC}] = (I + (1-\sigma)r_{RR}\mathbf{\Gamma}r_{C:P} + \kappa_{dC}[\text{DOC}] + \kappa_{\text{PIC}}[\text{PIC}] + F_{sea2air} + F_v[DIC]_g$$

$$\left[\frac{d}{dt} + \mathbf{T}\right][\text{DOC}] = \sigma\mathbf{\Gamma}r_{C:P} + \kappa_p[\text{POC}] - \kappa_{dC}[\text{DOC}]$$

$$\left[\frac{d}{dt} + \mathbf{F}_{\text{POC}}\right][\text{POC}] = (1-\sigma)\mathbf{\Gamma}r_{C:P} - \kappa_P[\text{POC}]$$

$$\left[\frac{d}{dt} + \mathbf{T}\right][\text{O}_2] = \mathbf{\Gamma}r_{O:P} - R_{\kappa_{dC}}[\text{DOC}]r_{O:C} - F_{sea2air}$$

$$\left[\frac{d}{dt} + \mathbf{T}\right][\text{ALK}] = -2(1-\sigma)r_{RR}\mathbf{\Gamma}r_{C:P} + r_{N:C}\mathbf{\Gamma}r_{C:P} - r_{N:C}\kappa_{dC}[\text{DOC}]$$
$$+ 2\kappa_P[\text{PIC}] + \kappa_g\left([\text{ALK}] - \overline{[\text{ALK}]}\right) + F_v[\text{ALK}]_g \qquad (3)$$

where $\mathbf{F}_{\text{POC}}$ and $\mathbf{F}_{\text{PIC}}$ are sinking flux divergence operators for particulate organic carbon (POC) and particulate inorganic carbon (PIC), respectively. $\mathbf{F}_{\text{POC}}$ is coded the same way as $\mathbf{F}_{\text{POP}}$ with an independent exponent b value (Table 2). $\mathbf{F}_{\text{PIC}}$ is coded to produce an exponential distribution curve for particulate inorganic carbon (PIC), the dissolution length scale (d) is optimized in the inversion. Dissolved inorganic carbon (DIC) assimilation rate is proportional to that of DIP ($\mathbf{\Gamma} \equiv \gamma[\text{DIP}]$) with a ratio ($r_{C:P}$) of carbon to phosphorus. Production allocation to particulate organic carbon (POC) and dissolved organic carbon (DOC) is determined using the same allocation factor as that in the phosphorus model (σ). The sea-to-air flux of CO_2 is modeled according to the formulation used for phase 2 of the Ocean Carbon-Cycle Model Intercomparison Project (OCMIP-2) (Najjar et al., 2007). PIC production rate is proportional to POC production rate with an adjustable parameter (r_{RR}: rain ratio, Table 2).

According to Redfield ratio, a mole of organic matter formation consumes 106 mol dissolved inorganic carbon (DIC) and 16 mol of NO_3^-. The conversion of 16 mol of NO_3^- to organic nitrogen consumes 16 mol H$^+$, thus increases total alkalinity by 16 mol ($r_{N:C}\mathbf{\Gamma}r_{C:P}$). Similarly, a mole of organic matter remineralization and nitrification leads to a reduction of total alkalinity of 16 mol ($r_{N:C}\kappa_{dC}[\text{DOC}]$). Dissolution of one mol PIC produces one mol CO_3^{2-}, thus leads to an increase of total alkalinity by two mol. PIC production functions in an opposite way. In addition, precipitation and evaporation can significantly impact surface ocean concentrations of DIC and alkalinity. To compensate these effects, we apply a virtual flux for DIC and ALK ($F_v[\text{DIC}]_g$ and $F_v[\text{ALK}]_g$, respectively, where $[\text{DIC}]_g$ and $[\text{ALK}]_g$ are surface ocean DIC and ALK mean concentration.) (Najjar et al., 2007).

Oxygen production is modeled to be proportional to DIP consumption with a ratio of oxygen to phosphorus ($r_{O:P}$), oxygen consumption is modeled to be proportional to dissolved organic carbon (DOC) remineralization rate with a ratio of oxygen to carbon ($r_{O:C}$).

$$\left[\frac{d}{dt} + \mathbf{T}\right][\text{O}_2] = \mathbf{\Gamma}r_{O:P} - R\kappa_{dC}[\text{DOC}]r_{O:C} - F_{sea2air} \qquad (4)$$

We use a hyperbolic function (R) to shut down oxygen consumption when oxygen level falls below a critical level, so that we prevent the model from producing negative oxygen concentrations

$$R = 0.5 + 0.5 \tanh\left[([O_2] - O_{crit})/[O_2]_0\right],$$

where O_{crit} is a critical oxygen concentration (10 mmol/L) below which oxygen consumption gradually decreases, and $[O_2]_0$ is set to 1 mmol/L and is used to remove dimension. Sea-to-air flux is modeled according to Ref (Najjar et al., 2007).

We sequentially solve the phosphorus, carbon and oxygen equations (Equations 2–4) based on an initial guess of parameter combinations. The difference between model results and observations is minimized by optimizing the model parameters in a Bayesian model frame (Wang et al., 2019). The observational constraints used in the model are DIP, DIC, ALK, and dissolved oxygen, which are obtained from GLODAPv2 data set, and interpolated into our model grid.

In our model, we assume that POC/POP is routed to DOC/DOP before getting remineralized to DIC/DIP. This scheme can prevent unrealistic accumulation of POC/POP at the bottom of high productivity waters and/or shallow waters since no sediment burial is permitted in the model. In this way, the process of parameter optimization is more stable than allowing POC/POP remineralized directly to DIC/DIP. Since our optimization routine can find optimal parameter combination to fit the observations, the different schemes produce similar results. In our model, the remineralization of POC to DIC and POP to DIP is decoupled by the different values of k_{dc} and k_{dp}. Such decoupled remineralizations of POM and DOM were also documented in previous study (e.g., Kwon et al., 2022; Loh & Bauer, 2000).

2.2. Model Validation

In the model, we optimized a suite of biogeochemical parameters and attempted to generate state-of-the-art biogeochemical estimates. The equilibrated tracers are highly consistent with observations (e.g., DIP, DIC, ALK, O_2) (Figure 1). In addition, spatial pattern of the distribution of surface phosphate shows close agreement with the WOA2013 data regarding spatial patterns (Figure 2).

2.3. Sensitivity Tests

In the sensitivity tests, we perturb the optimal model by adjusting production in HNLCs. We increase DIP/DIC uptake rate so that nutrients in the surface ocean can be quickly drawn down in HNLCs. Because the phosphorus model is linear and there are no interactions with the atmosphere, we thus solve the steady state solution after perturbation using direct matrix inversion. For the carbon module, we add a one-box atmospheric layer on top of our ocean model and assume that the carbon is conserved in the system. Therefore, the overall uptake of CO_2 by the ocean leads to a decrease of CO_2 in the atmosphere. To find the steady-state solution, we do a transient run on the coupled atmosphere and ocean model with a time step of 1/20 years. We integrated the perturbed model until it reached a new equilibrium state. The timescale depends on the specific perturbation in the HNLC regions (Figure 3). It takes 3,100, 2,400, and 2,100 years to reach a new equilibrium state for the SOxN, NPxN and EPxN, respectively. The strong exchange of carbon between atmosphere and ocean occurs in the first 500–1,000 years. For the oxygen model, we use steady-state solutions after perturbation from phosphorus and carbon models as inputs and solve the oxygen model using Newton's method.

3. Results

A series of sensitivity experiments are performed by increasing the productivity in these HNLC regions whose boundaries are delineated in Figure 2. In this study, we do not attempt to explore the exact limiting factors of productivity in the HNLCs. Instead, we focus primarily on the consequences of elevated productivity in these sensitivity runs. The productivity is increased by adjusting a parameter (α) in the biological uptake term of Equation 2. We perform a series of sensitivity experiments by increasing the nutrient uptake rate to different levels in Equation 2. When the biological uptake rate is elevated to a level strong enough that biological pump can quickly draw down the nutrient of upper ocean, we refer to the final experiments in the Southern Ocean, subarctic North Pacific and equatorial Pacific Ocean as SO × N, NP × N and EP × N, respectively (Table 1). The N here

Table 1

The Change of Atmospheric CO₂ (ppm), Global Mean Oxygen (μM), Volume of Oxygen Minimum Zones (10⁷ km³), and the Efficiency of Soft Tissue Pump in the Control and Sensitivity Runs

Experiments	P* (soft tissue pump efficiency)	Atmospheric CO₂ drawdown (ppm)/ (Percent)	Global mean oxygen (μM)	Volume of oxygen minimum zones (<30 μM) (10⁷ km³)
Ctrl	0.37 (0.36)	0.0	171.2 (169.8)	2.7 (3.0)
SO×N	0.51	45.1 (16.2%)	135.1	11.8
EP×N	0.38	3.4 (1.2%)	168.9	3.4
NP×N	0.39	6.7 (2.4%)	167.1	4.4
ALL×N	0.54	52.3 (18.7)	125.5	16.9

Note. For the control run, values obtained from the WOA13 data are indicated in parenthesis.

indicates that biological uptake rate is N times larger than in the control run. For the current model setup and optimized parameters, N is about 50. We also conduct an experiment with the productivity increased simultaneously in all three HNLCs, which is referred to as ALL × N.

3.1. Increased Productivity in the Southern Ocean

The SO × N experiment assumes highly efficient nutrient removal by the ecosystem in the Southern Ocean. Thus, the elevated biological uptake of DIP in the surface layer produces a strong negative DIP perturbation relative to the control run (Figures 4a and 4d). Elevated production also causes massive transport of nutrients into deep layers of the Southern Ocean, where the waters with more respired nutrients are advected northward in the bottom ocean and can arrive at 60°N. At the same time, decreased DIP concentrations are revealed in the surface and intermediate depths north of 40°S. Less nutrient in the surface waters would decrease photosynthesis and reduce regenerated DIP below the surface, which intensifies the negative anomaly in the intermediate waters. The loss of nutrients in these waters compensates the nutrient gain in the Southern Ocean and global deep ocean. Similar nutrient redistribution was reported in previous studies (Joos, Siegenthaler, & Sarmiento, 1991; Laufkotter & Gruber, 2018; Marinov et al., 2006; Moore et al., 2018; Sarmiento & Orr, 1991) when the productivity in the Southern Ocean was increased. These studies used relatively short-term model simulations (100–300 years), at the end of which the model is still strongly evolving (Figure 3). Therefore, our results provide conclusive evidence of the impact of the Southern Ocean nutrient removal on the shift of global nutrient distribution.

Highly elevated production in the Southern Ocean redistributes the nutrients in the ocean (Figures 4b and 4e). The DIP inventory shows a widespread cumulation of nutrients in the Southern Ocean, a large fraction of the Indian Ocean, and nearly the whole Pacific Ocean in the north hemisphere (Figure 4e). The loss of nutrients occurs in the whole Atlantic Ocean and the southeast Pacific Ocean. The distribution of the DIP inventory perturbation exhibits the connections between different ocean basins to the Southern Ocean. In addition, the redistribution of nutrients changes the efficiency of global biological pump. Following Ito and Follows (2005), we quantify the efficiency of soft tissue pump (P* in their study) by using the ratio between global mean regenerated phosphate and global mean phosphate. Regenerated phosphate, P_{reg}, is here defined as the phosphate that results from the remineralization of organic matter that is produced biologically at the surface and then carried into the interior in dissolved organic form by water parcels and by sinking particulate organic matter. By definition, P_{reg} is given by $P_{reg} = AOU/R_{o2:P}$, where AOU is apparent oxygen utilization. In the global ocean, P* was increased from 0.37 to 0.51 (Table 1), clearly indicating more nutrients transported to the deep ocean by the export and remineralization of organic material.

Global zonal average DIC displays similar patten on the latitude-depth section (Figure 4c). Negative DIC perturbation is found in the upper layer of the Southern Ocean as compared to the control run. This helps to reduce pCO₂ in the Southern Ocean and enhance oceanic uptake of atmospheric CO₂. Deep ocean waters exhibit large positive DIC perturbation due to an enhanced biological pump. Note that these deep waters with excessive DIC could make up for the disequilibrium caused by the elevated productivity when they had contacted with the surface waters in the Southern Ocean on a time scale of a few millennia with changing circulation. The DIC inventory perturbation (Figure 4f) shows similar pattern to that of the DIP. DIC inventory is increased in regions where positive DIP perturbations are found. In the Atlantic Ocean, we find very minor change in DIC inventory despite the reduction of nutrients. This may be attributed to the fact that the surface nutrient concentrations of these areas are already low. In total, the ocean carbon uptake is increased by 96 Pg C, which is equivalent to a reduction of 45.1 ppm in atmospheric CO₂ concentration (Table 1).

The pattern of global zonal mean oxygen mirrors that of the DIP on the latitude-depth section (Figure 4c). Oxygen in the intermediate waters of 150–600 m is increased due in part, to the advection down from high latitude surface waters where it is produced by photosynthesis and in part to the reduced intermediate water regeneration noted in the DIP distribution. The relative role of advection and reduced regeneration of DIP was quantified in Fu et al. (2018), which showed that the impact of advection is relatively small for the increased oxygen. Most

Table 2
Optimal Model Parameters With Their Uncertainties ($\pm\sigma$). σ is Production Allocation Parameter, κ_{dP} and κ_{dC} Are Dissolved Organic Phosphorus and Dissolved Organic Carbon Remineralization Rate Constants, Respectively

Parameters	Optimal value $\pm$ 1σ	Units
σ	$0.23^{+0.02}_{-0.02}$	Unitless
κ_{dP}	$2.17^{+0.09}_{-0.08} \times 10^{-8}$	s^{-1}
b_P	$1.15^{+0.003}_{-0.003}$	Unitless
α	$5.43^{+0.16}_{-0.14} \times 10^{-8}$	s^{-1}
β	$0.21^{+1.80}_{-0.19} \times 10^{-4}$	Unitless
b_C	$1.18^{+0.002}_{-0.002} \times 10^{-1}$	Unitless
d	$4057.34^{+20.59}_{-20.49}$	m
κ_{dC}	$5.78^{+0.21}_{-0.21} \times 10^{-8}$	s^{-1}
r_{RR}	$2.67^{+0.01}_{-0.01} \times 10^{-2}$	Unitless
cc	$1.81^{+Inf}_{-1.81} \times 10^{-9}$	L μM^{-1}
dd	$6.24^{+0.03}_{-0.03} \times 10^{-3}$	Unitless
$r_{O:C}$	$1.24^{+0.01}_{-0.01}$	Unitless
$r_{O:P}$	$182.70^{+1.53}_{-1.52}$	Unitless
κ_p	3.86×10^{-7}	s^{-1}

Note. b_P and b_C are Martin curve exponents for particulate organic phosphorus and particulate organic carbon (POC), respectively. α and β are defined in Equation 2. d is particulate inorganic carbon (PIC) dissolution length scale. r_{RR} is PIC to POC production ratio. cc and dd are two parameters that define P:C (or C:P) assimilation rate ($r_{C:P} = 1/(cc[DIP] + dd)$). $r_{O:C}$ and $r_{O:P}$ are oxygen to carbon ratio and oxygen to phosphorus ratio, respectively.

deep water is deoxygenated except north high latitudes (>60°N), reflecting increased accumulation of respired carbon. Deep-water deoxygenation expands the hypoxic waters in the deep Pacific Ocean. Global mean oxygen concentration is decreased by 15% (26.1 μM) relative to the control run (Table 1). Oxygen inventory is decreased in most of the global ocean except high-latitude North Atlantic and the Arctic Ocean (Figure 4g). In the Southern Ocean and North Pacific, the oxygen inventory is significantly decreased by 300 mol/m². Meanwhile, the simulated global volume of hypoxic waters is more than 4 times larger than the control run, suggesting a more severe environment for marine animals (Table 1).

3.2. Increased Productivity in the Equatorial/North Pacific

When productivity is elevated in the eastern equatorial Pacific, the depth-latitude section presents positive DIP perturbations within the 300–2,000 m depth range between 30°S–30°N (Figure 5a) while surface DIP is drawn down (Figure 5d). In contrast to the case of the Southern Ocean, negative perturbations are found in most of the deep ocean (below 2,000 m). For the North Pacific case (Figure 6a), maximum positive perturbations occur from 200 to 1,000 m and centered at 45°N. The positive perturbation (DIP increases) extends from 200 m to the bottom and southward at 1,000 m to 30°S, probably related to the North Pacific Intermediate Water (Sarmiento et al., 2004). Surface DIP is decreased mostly in the North Pacific and eastern equatorial Pacific (Figure 6d). As for DIP inventory (Figure 5e), large positive perturbations are confined to the eastern Pacific in the EP × N run. The magnitude of perturbations diminishes from the eastern to central Pacific. The positive changes are accompanied by negative perturbations occurring in the north Indian Ocean and tropical Atlantic Ocean (Figure 5e). For the NP × N run, positive perturbations are stronger than the EP × N, extending from North Pacific to 30°S while the rest of ocean shows negative perturbations (Figure 6e).

DIC perturbations present similar patterns to the DIP (Figures 5c and 5f; Figures 6c and 6f) with positive signals coinciding with those of the DIP. Globally, the increases of P* in both runs indicate enhanced efficiency of soft tissue pump. The increase of ocean carbon inventory is equivalent to a CO_2 drawdown of 3.4 and 6.7 ppm from the atmosphere in the EP × N and NP × N run, respectively. The change of ocean carbon uptake in these runs are much smaller than the SO × N. Equatorial Pacific waters are isolated from the vast bulk of the ocean due to their low density. As a result, the impact of elevated productivity is primarily confined to the local regions where the productivity is increased. The impact in the North Pacific is relatively larger compared to the equatorial band, presumably because the North Pacific exchanges with a larger volume of water contained in the main thermocline.

In both EP × N and NP × N runs, global mean oxygen concentration is decreased slightly by 2.3 and 4.1 μM, respectively In the EP x N run, the decrease of oxygen inventory in the eastern Pacific is compensated by other regions (Figure 5g). In the NP x N run, similarly, the decrease of oxygen inventory occurs mostly in the North Pacific while oxygen inventory is increased in other regions (Figure 6g). More hypoxic waters are developed in the NP × N run than the EP × N run especially in the mid-latitude central North Pacific. As a result, a larger oxygen minimum zone (OMZ) is seen, whose volume is increased by 26% and 63% in the EP × N and NP × N run, respectively. Our results demonstrate that a globally more efficient biological pump would result in ocean deoxygenation.

If we increase the productivity in all three HNLC regions, the efficiency of soft tissue pump is increased by 46% (0.54), leading to a drawdown of atmospheric CO_2 of 52.3 ppm. The global mean dissolved oxygen is decreased by 27%–125.5 μM, accompanied by an expanded oxygen minimum zone (OMZ) volume that is 6 times larger than in the control run (Table 1).
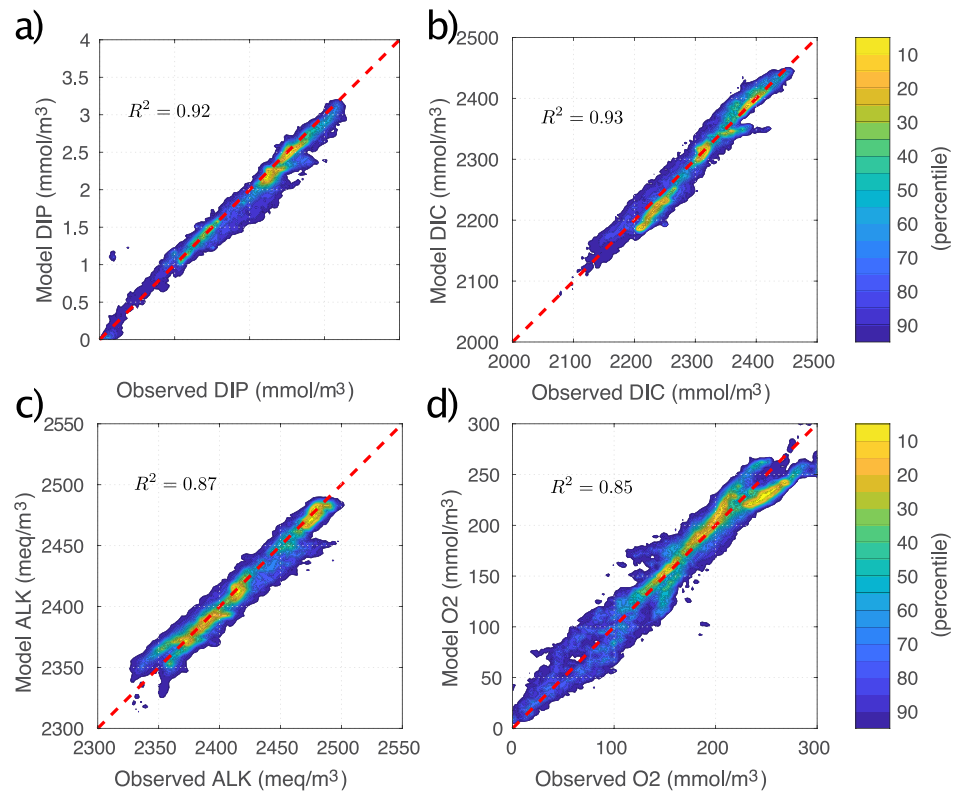
Figure 1. Tracer-tracer comparisons between our optimal model results and observations downloaded from GLODAPv2 website (https://www.glodap.info). The red dash line in each figure shows 1:1 line, and the colormap indicates distribution of percentile.
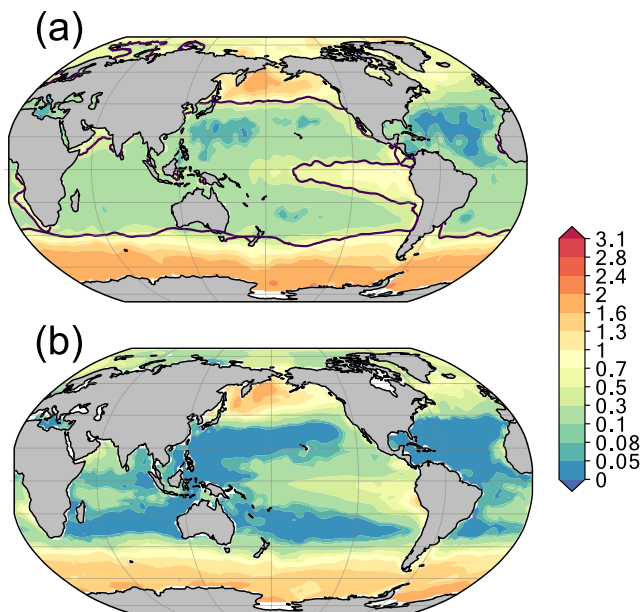
4. Conclusion and Discussion

Increases of productivity in the HNLC regions by iron fertilization is thought to be a geoengineering approach to reduce atmosphere CO_2 concentration. While more carbon is absorbed into the ocean, it takes several thousand years before a new equilibrium atmosphere CO_2 level is achieved. The long-time scale makes it difficult to determine the fate of the absorbed carbon and evaluate its final impact on climate. To explore the impact of the fertilization experiments, we use an optimized biogeochemical inverse model to investigate the equilibrium responses of global ocean to increased productivity in three major HNLC regions. We set the atmospheric CO_2 to a preindustrial level of 278 ppm and assume total carbon conservation in the ocean and atmosphere.

We increased the productivity and hence micronutrient uptake rate by 50 times in the HNLC regions to explore the maximum potential of ocean iron fertilization (OIF) in mitigating climate warming. The 50 times is higher than the productivity change in the actual OIFs conducted since 1990s (Yoon et al., 2018). In the read-world OIFs, the productivity was increased by 2 times to more than 10 times after iron addition, suggesting highly uncertain outcomes. In the OIFs in the Southern Ocean, 10 times increase in productivity can draw down up to 30% of surface DIP. Larger increases in the productivity are expected to produce a stronger DIP drawdown. Therefore, 50 times increase in uptake rate seems reasonable for a relatively complete drawdown of surface DIP in this study.
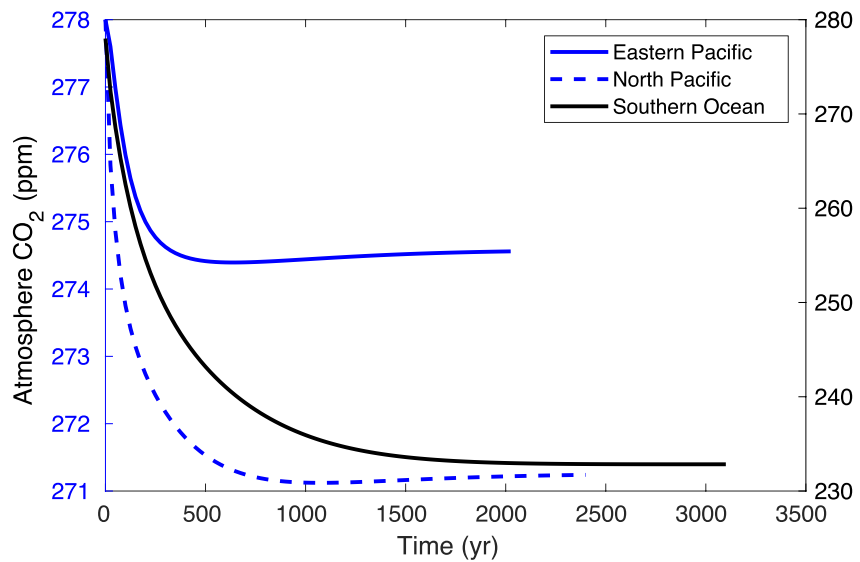

Figure 2. Surface dissolved inorganic phosphorus (mmol/m³) of (a) WOA18 data and (b) OCIM. The boundary of three major high nutrient low chlorophyll regions was delineated with a black line.

Figure 3. The timescale for the atmosphere CO_2 to reach a new equilibrium after the productivity is increased in the Southern Ocean, North Pacific and eastern equatorial Pacific.

In the Southern Ocean HNLC, increased productivity removes nutrients from surface waters. The deep circumpolar waters are enriched in nutrients by regeneration of organic matter, which results in an overall downward shift of nutrients and carbon from surface and intermediate to circumpolar and deep waters. The efficiency of soft tissue pump is increased by 38%, which overcompensates the reduction of low-latitude new production. Total oceanic carbon uptake is increased by 96 Pg C (45.1 ppm CO_2 from atmosphere). The increases of carbon are mostly stored in the Southern Ocean, Indian and Pacific Ocean of the north hemisphere. Increased productivity in the equatorial and North Pacific HNLCs also shifts more nutrients and carbon downward from surface and intermediate to deep waters. However, the impact is more restricted to the regions close to the perturbation regions. The efficiency of soft tissue pump is increased by 3% and 5.4%, resulting in carbon uptake of 3.4 Pg C and 6.7 Pg C, respectively.

Increased productivity in the Southern Ocean, equatorial Pacific and North Pacific HNLC decreases global mean dissolved oxygen by 21%, 1.3% and 3.0%, respectively. The oxygen content shifts upward in the water column, approximately mirroring the downward shift of nutrients. More hypoxic waters are developed in the global ocean. In particular, the high productivity in the Southern Ocean produces an oxygen minimum zone (OMZ) volume that is 4 times larger than the control run. The OMZ volume is increased by 26% and 63% in the Equatorial and North pacific case, respectively.

The expanded oxygen minimum zones (OMZs) suggests increased emissions of climate-relevant gases such as N_2O (Martinez-Rey et al., 2015). N_2O has a relatively long lifetime in the atmosphere (~110 years) and a global warming potential about 310 times greater than CO_2 (Forster et al., 2007). Therefore, the expansion of oxygen minimum zones (OMZs) is expected to, in the long run, contribute to an increase in the greenhouse effect (Fuhrman & Capone, 1991). For example, the increases of productivity in all the HNLC regions results in an OMZ volume that is 6 times larger than the control run. We relate the increase in the N_2O production to the modeled increase in export production according to Fuhrman and Capone (1991). In the ALLxN run, export production is increased by a mean of 120%. Multiplying the current emissions of N_2O by the increase in export production yields an increased emission of N_2O of 4.4 Tg N yr^{-1}. This simple estimate is about 35% of the total N_2O emissions from global land ecosystems, which was estimated to be 12.52 ± 0.74 Tg N/yr during 1981–2010 (Tian et al., 2017). The change in N_2O emission can be converted to an equivalent amount of CO_2 emission by multiplying a factor of 310 and by the carbon content of CO_2 (12/44) to yield 0.37 Pg C/yr. The estimated N_2O emission has important implication for climate warming. Current ocean anthropogenic carbon uptake is 2.5 ± 0.6 Pg C/yr based on the 2019 assessment of the Global Carbon Project. If we assume that the large-scale OIF as in the AllxN occurs in the real ocean, the increase of N_2O can offset the impact of CO_2 drawdown on climate warming by a maximum of 19%.
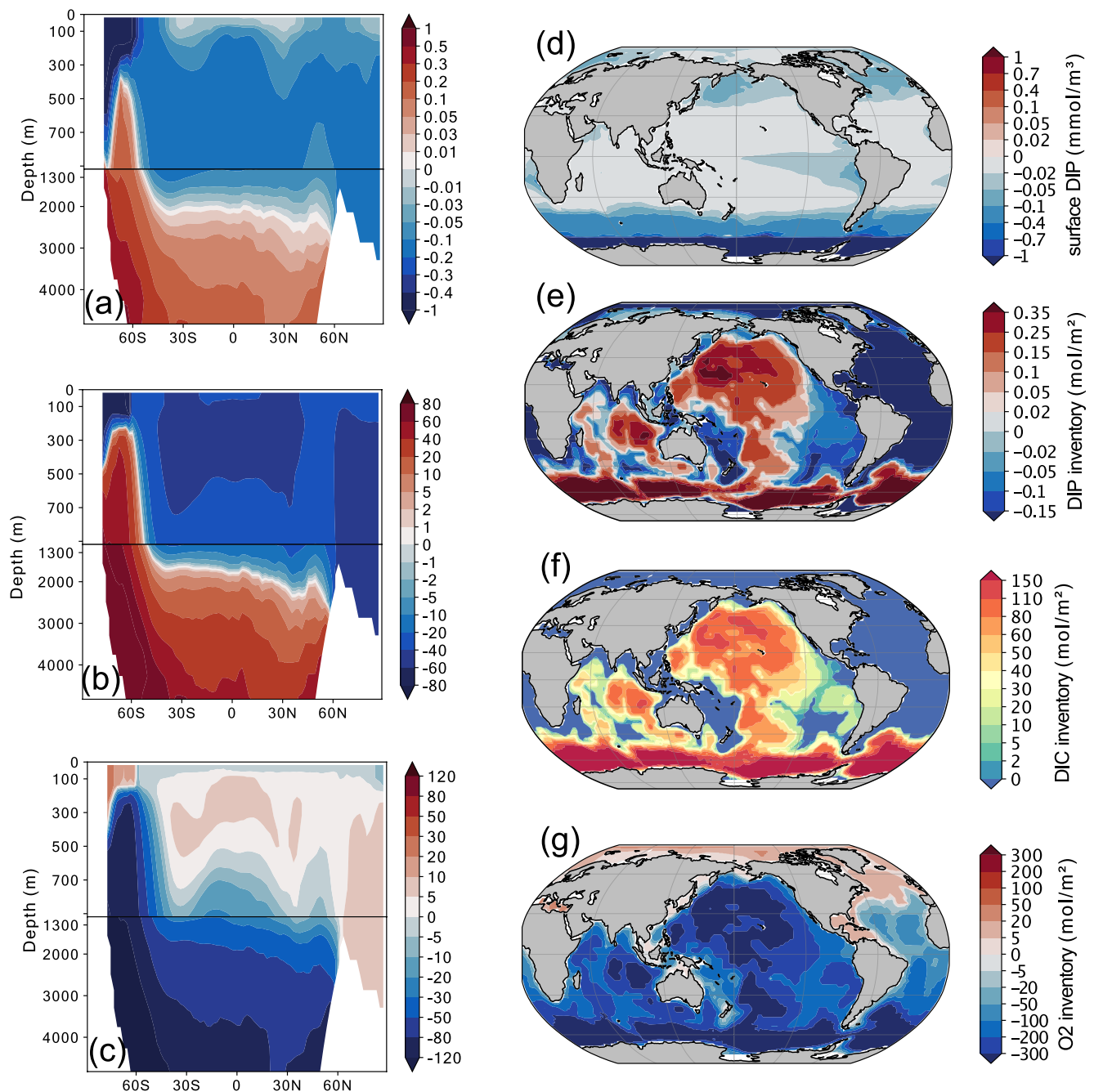
Figure 4. Depth-latitude sections of global zonal mean difference between the SO × N and control run are shown for (a) Dissolved inorganic phosphorus (DIP) (mmol/m³), (b) Dissolved inorganic carbon (DIC) (mmol/m³) and (c) dissolved oxygen (mmol/m³). The difference of surface DIP is shown in (d) and the differences of column inventory are shown for (e) DIP and (f) DIC and (g) dissolved oxygen.

The question of whether artificial OIF is a viable carbon removal strategy is still under debate (Boyd et al., 2007; Emerson, 2019; Lauderdale et al., 2020; Smetacek & Naqvi, 2008; Yoon et al., 2018). Major concerns include the decline of oxygen inventory, the production of N_2O emissions and detrimental environment impact. Regarding ocean carbon sequestration, our results show a maximum reduction of 18.7% of the preindustrial atmospheric CO_2 concentration (278 ppm) with 50 times increase in productivity in all three major HNLCs. This seems promising to mitigate climate warming, but it should be noted that the 50 times increases of productivity is likely too high in the real ocean (Yoon et al., 2018) and might not be achieved for large-scale IOFs. In addition, the efficacy of OIF will be offset by continuous anthropogenic CO_2 emissions, which is driving up ocean surface
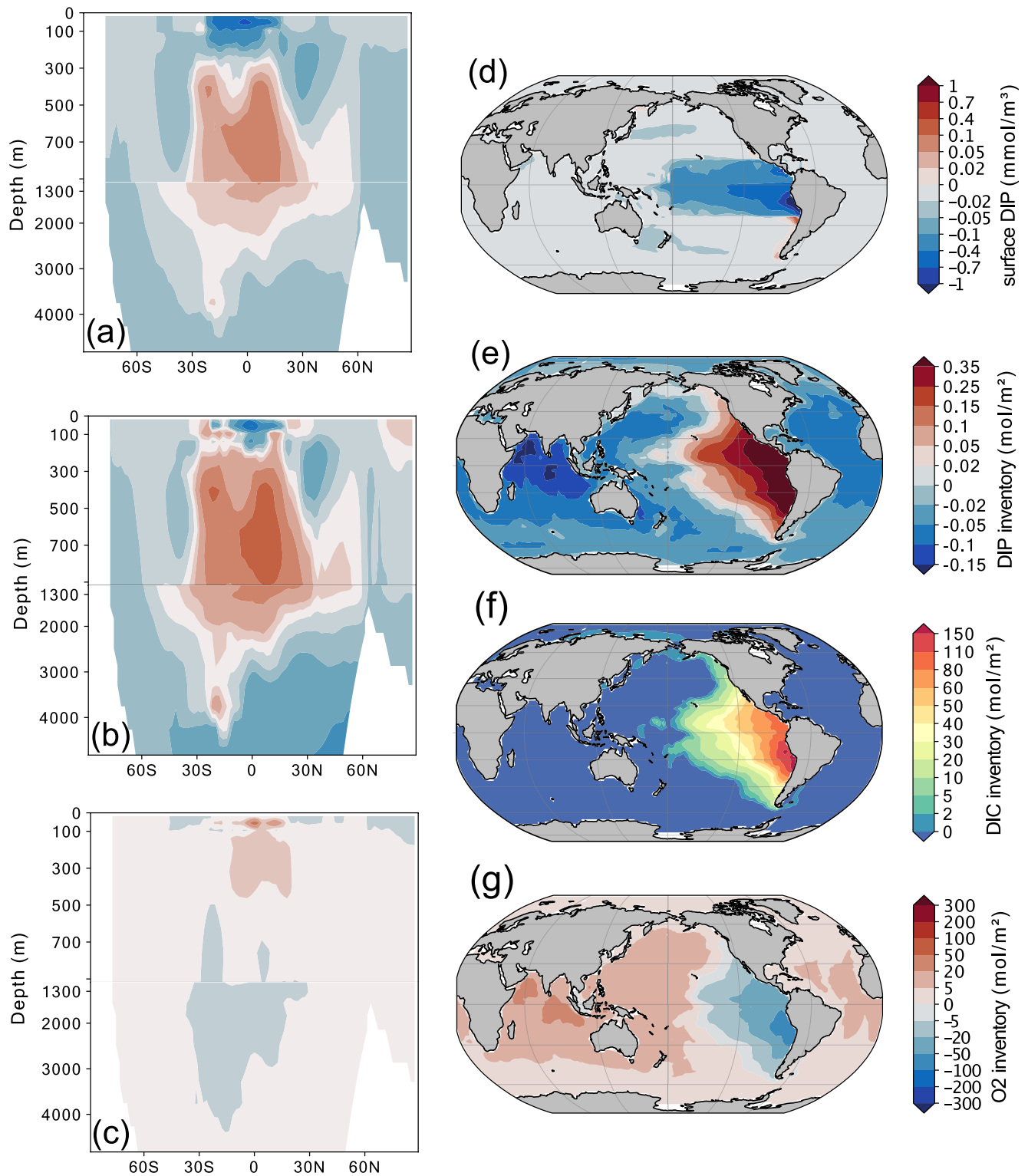
Figure 5. Depth-latitude sections of global zonal mean difference between the EP × N and control run are shown for (a) Dissolved inorganic phosphorus (DIP) (mmol/m³), (b) Dissolved inorganic carbon (DIC) (mmol/m³) and (c) dissolved oxygen (mmol/m³). The difference of surface DIP is shown in (d) and the differences of column inventory are shown for (e) DIP and (f) DIC and (g) dissolved oxygen.
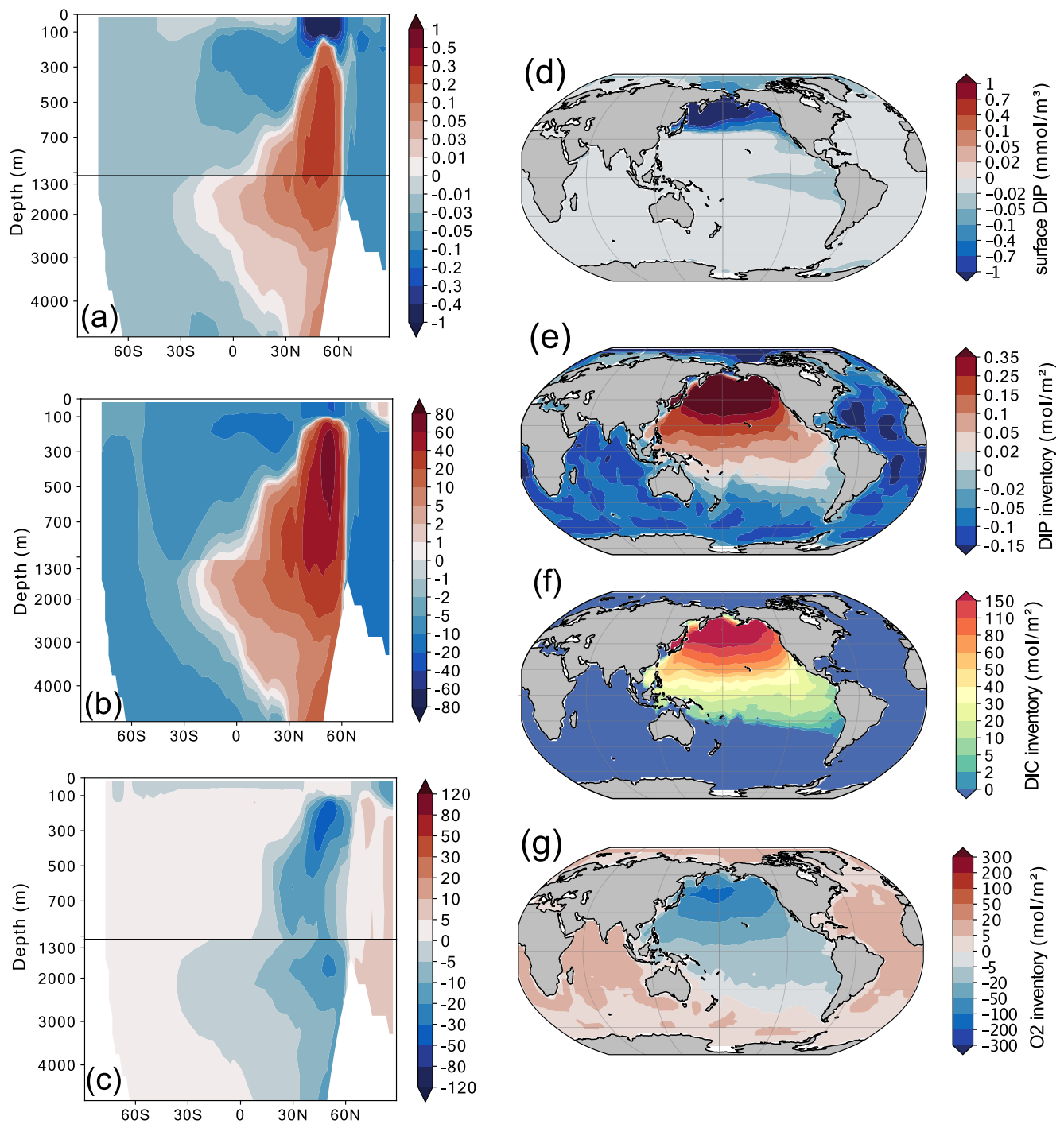
Figure 6. Similar to Figure 5 but for the NP × N.

temperatures and causing ocean acidification (Caldeira & Wickett, 2003). Both ocean warming and acidification can diminish the capacity of ocean carbon uptake. Previous study also demonstrated that changes in calcium carbon production with macronutrient fertilization could significantly reduce carbon sequestration efficiency. When calcium carbonate production increases at the same rate as export production, the carbon sequestration efficiency is reduced by 25% (Matear & Elliott, 2004). Therefore, a drawdown of atmosphere CO_2 will be less than 18.7% for future warming scenarios. Even if we ignore other climate related gases such as N_2O, which can

modify the efficacy of carbon sequestration by 19%, it seems difficult for the Fe fertilization strategy to achieve the model outcome in real ocean.

A drawback of the biogeochemical inverse model in this study is that the model considers some simplified biogeochemical processes. For example, we assume that POC/POP is routed to DOC/DOP before getting remineralized to DIC/DIP. In the real ocean, however, a proportion of POC/POP is directly remineralized to DIC/DIP. To test how our assumption of POC/POC routed to DOC/DOP can affect our results, we ran another model in which POC/POP was directly remineralized to DIC/DIP. The process of optimizing parameters became unstable, and we needed to fix the fraction (σ) of production routed to dissolved and particulate form. Nevertheless, we were able to obtain very similar DIP, DIC, ALK, and oxygen distributions to the original model setup. Global mean oxygen concentration is 170.1 mmol/m^3 as compared to 171.2 mmol/m^3 reported in original control run. A similar SOxN run also produced very similar results to those in Figure 3 (figure not shown). Therefore, our model setup is appropriate to investigate the responses to perturbations in different HNLCs.

We are aware that the productivity change in HNLCs also depends on other factors, such as meso-zooplankton grazing rates, light and initial silicate concentrations (Yoon et al., 2018). We here focus on the long-term impact of increased productivity on ocean carbon sequestration and the change of oxygen inventory. Our results confirm that more organic matter is eventually transported out of surface ocean and stored in the deep ocean after ~1,000 years. A decrease of 18.7% CO_2 in the atmosphere implies that OIF is a useful a geoengineering tool to slow down climate warming. However, the significant development of hypoxia poses serious threat to marine environment. Some important issues need to be further explored, like the efficacy of OIF with increasing anthropogenic CO_2 and climate warming and the quantification of negative effects of OIF such as declines in oxygen content and production of climate-relevant gases.

Conflict of Interest

The authors declare no conflicts of interest relevant to this study.

Data Availability Statement

Model simulations used this study can be accessed via: https://doi.org/10.5281/zenodo.5915669.

References

Blain, S., Quéguiner, B., Armand, L., Belviso, S., Bombled, B., Bopp, L., et al. (2007). Effect of natural iron fertilization on carbon sequestration in the southern ocean. *Nature*, *446*(7139), 1070–1074. https://doi.org/10.1038/nature05700

Boyd, P. W., Jickells, T., Law, C. S., Blain, S., Boyle, E. A., Buesseler, K. O., et al. (2007). Mesoscale iron enrichment experiments 1993–2005: Synthesis and future directions. *Science*, *315*(5812), 612–617. https://doi.org/10.1126/science.1131669

Brown, M. S., Munro, D. R., Feehan, C. J., Sweeney, C., Ducklow, H. W., & Schofield, O. M. (2019). Enhanced oceanic co2 uptake along the rapidly changing West Antarctic Peninsula. *Nature Climate Change*, *9*(9), 678–683. https://doi.org/10.1038/s41558-019-0552-3

Caldeira, K., & Duffy, P. B. (2000). The role of the southern ocean in uptake and storage of anthropogenic carbon dioxide. *Science*, *287*(5453), 620–622. https://doi.org/10.1126/science.287.5453.620

Caldeira, K., & Wickett, M. E. (2003). Anthropogenic carbon and ocean pH. *Nature*, *425*(6956), 365. https://doi.org/10.1038/425365a

DeVries, T., & Holzer, M. (2019). Radiocarbon and helium isotope constraints on deep ocean ventilation and mantle-^{3}He sources. *Journal of Geophysical Research: Oceans*, *124*(5), 3036–3057. https://doi.org/10.1029/2018jc014716

DeVries, T., Holzer, M., & Primeau, F. (2017). Recent increase in oceanic carbon uptake driven by weaker upper-ocean overturning. *Nature*, *542*(7640), 215–218. https://doi.org/10.1038/nature21068

Emerson, D. (2019). Biogenic iron dust: A novel approach to ocean iron fertilization as a means of large scale removal of carbon dioxide from the atmosphere. *Frontiers in Marine Science*, *6*. https://doi.org/10.3389/fmars.2019.00022

Forster, P., Ramaswamy, V., Artaxo, P., Berntsen, T., Betts, R., Fahey, D. W., et al. (2007). In S. Solomon, D. Qin, M. Manning, Z. Chen, M. Marquis, K. B. Averyt, M. Tingor, & H. L. Miller (Eds.), *Climate change 2007: The physical science basis. Contribution of working group i to the fourth assessment report of the intergovernmental panel on climate change*(pp. 129–234). Cambridge University Press.

Frost, B. W. (1991). The role of grazing in nutrient-rich areas of the open sea. *Limnology & Oceanography*, *36*(8), 1616–1630. https://doi.org/10.4319/lo.1991.36.8.1616

Fu, W. W., Primeau, F., Keith Moore, J., Lindsay, K., & Randerson, J. T. (2018). Reversal of increasing tropical ocean hypoxia trends with sustained climate warming. *Global Biogeochemical Cycles*, *32*(4), 551–564. https://doi.org/10.1002/2017gb005788

Fuhrman, J. A., & Capone, D. G. (1991). Possible biogeochemical consequences of ocean fertilization. *Limnology & Oceanography*, *36*(8), 1951–1959. https://doi.org/10.4319/lo.1991.36.8.1951

Gaspari, V., Barbante, C., Cozzi, G., Cescon, P., Boutron, C. F., Gabrielli, P., et al. (2006). Atmospheric iron fluxes over the last deglaciation: Climatic implications. *Geophysical Research Letters*, *33*(3). https://doi.org/10.1029/2005gl024352

Gruber, N., Landschützer, P., & Lovenduski, N. S. (2019). The variable southern ocean carbon sink. *Annual Review of Marine Science*, *11*, 159–186. https://doi.org/10.1146/annurev-marine-121916-063407

Ito, T., & Follows, M. J. (2005). Preformed phosphate, soft tissue pump and atmospheric CO_2. *Journal of Marine Research*, *63*(4), 813–839. https://doi.org/10.1357/0022240054663231

Joos, F., Sarmiento, J. L., & Siegenthaler, U. (1991). Estimates of the effect of southern-ocean iron fertilization on atmospheric CO_2 concentrations. *Nature*, *349*(6312), 772–775. https://doi.org/10.1038/349772a0

Joos, F., Siegenthaler, U., & Sarmiento, J. L. (1991). Possible effects of iron fertilization in the southern ocean on atmospheric CO_2 concentration. *Global Biogeochemical Cycles*, *5*(2), 135–150. https://doi.org/10.1029/91gb00878

Keller, D. P., Feng, E. Y., & Oschlies, A. (2014). Potential climate engineering effectiveness and side effects during a high carbon dioxide-emission scenario. *Nature Communications*, *5*, 3304. https://doi.org/10.1038/ncomms4304

Kohfeld, K. E., Quéré, C. L., Harrison, S. P., & Anderson, R. F. (2005). Role of marine biology in glacial-interglacial CO_2 cycles. *Science*, *308*(5718), 74–78. https://doi.org/10.1126/science.1105375

Kurz, K. D., & Maierreimer, E. (1993). Iron fertilization of the austral ocean—The Hamburg model assessment. *Global Biogeochemical Cycles*, *7*(1), 229–244. https://doi.org/10.1029/92gb02910

Kwon, E. Y., Holzer, M., Timmermann, A., & Primeau, F. (2022). Estimating three-dimensional carbon-to-phosphorus stoichiometry of exported marine organic matter. *Global Biogeochemical Cycles*, e2021GB007154. https://doi.org/10.1029/2021gb007154

Landschutzer, P., Gruber, N., Bakker, D. C. E., & Schuster, U. (2014). Recent variability of the global ocean carbon sink. *Global Biogeochemical Cycles*, *28*(9), 927–949. https://doi.org/10.1002/2014gb004853

Lauderdale, J. M., Braakman, R., Forget, G., Dutkiewicz, S., & Follows, M. J. (2020). Microbial feedbacks optimize ocean iron availability. *Proceedings of the National Academy of Sciences of the United States of America*, *117*(9), 4842–4849. https://doi.org/10.1073/pnas.1917277117

Laufkotter, C., & Gruber, N. (2018). Will marine productivity wane? *Science*, *359*(6380), 1103–1104. https://doi.org/10.1126/science.aat0795

Loh, A. N., & Bauer, J. E. (2000). Distribution, partitioning and fluxes of dissolved and particulate organic c, n and p in the eastern north pacific and southern oceans. *Deep-Sea Research Part I-Oceanographic Research Papers*, *47*(12), 2287–2316. https://doi.org/10.1016/s0967-0637(00)00027-3

Marinov, I, Gnanadesikan, A., Toggweiler, J. R., & Sarmiento, J. L. (2006). The southern ocean biogeochemical divide. *Nature*, *441*(7096), 964–967. https://doi.org/10.1038/nature04883

Martin, J. H. (1990). Glacial-interglacial CO_2 change: The iron hypothesis. *Paleoceanography*, *5*(1), 1–13. https://doi.org/10.1029/pa005i001p00001

Martinez-Rey, J., Bopp, L., Gehlen, M., Tagliabue, A., & Gruber, N. (2015). Projections of oceanic N_2O emissions in the 21st century using the IPSL Earth system model. *Biogeosciences*, *12*(13), 4133–4148. https://doi.org/10.5194/bg-12-4133-2015

Matear, R. J., & Elliott, B. (2004). Enhancement of oceanic uptake of anthropogenic CO2 by macronutrient fertilization. *Journal of Geophysical Research-Oceans*, *109*(C4). https://doi.org/10.1029/2000jc000321

Mitchell, B. G., & Holmhansen, O. (1991). Biooptical properties of Antarctic Peninsula waters—Differentiation from temperate ocean models. *Deep-Sea Research Part a-Oceanographic Research Papers*, *38*(8–9), 1009–1028. https://doi.org/10.1016/0198-0149(91)90094-v

Moore, J. K., Fu, W., Primeau, F., Britten, G. L., Lindsay, K., Long, M., et al. (2018). Sustained climate warming drives declining marine biological productivity. *Science*, *359*(6380), 1139–1143. https://doi.org/10.1126/science.aao6379

Najjar, R. G., Jin, X., Louanchi, F., Aumont, O., Caldeira, K., Doney, S. C., et al. (2007). Impact of circulation on export production, dissolved organic matter, and dissolved oxygen in the ocean: Results from phase ii of the ocean carbon-cycle model intercomparison project (OCMIP-2). *Global Biogeochemical Cycles*, *21*(3), GB3007. https://doi.org/10.1029/2006gb002857

Oschlies, A., Koeve, W., Rickels, W., & Rehdanz, K. (2010). Side effects and accounting aspects of hypothetical large-scale southern ocean iron fertilization. *Biogeosciences*, *7*(12), 4017–4035. https://doi.org/10.5194/bg-7-4017-2010

Peng, T. H., & Broecker, W. S. (1991). Dynamic limitations on the Antarctic iron fertilization strategy. *Nature*, *349*(6306), 227–229. https://doi.org/10.1038/349227a0

Pitchford, J. W., & Brindley, J. (1999). Iron limitation, grazing pressure and oceanic high nutrient-low chlorophyll (HNLC) regions. *Journal of Plankton Research*, *21*(3), 525–547. https://doi.org/10.1093/plankt/21.3.525

Primeau, F. W., Holzer, M., & DeVries, T. (2013). Southern ocean nutrient trapping and the efficiency of the biological pump. *Journal of Geophysical Research-Oceans*, *118*(5), 2547–2564. https://doi.org/10.1002/jgrc.20181

Rae, J. W. B., Burke, A., Robinson, L. F., Adkins, J. F., Chen, T., Cole, C., et al. (2018). CO2 storage and release in the deep southern ocean on millennial to centennial timescales. *Nature*, *562*(7728), 569–573. https://doi.org/10.1038/s41586-018-0614-0

Sarmiento, J. L., Gruber, N., Brzezinski, M. A., & Dunne, J. P. (2004). High-latitude controls of thermocline nutrients and low latitude biological productivity. *Nature*, *427*(6969), 56–60. https://doi.org/10.1038/nature02127

Sarmiento, J. L., & Orr, J. C. (1991). 3-dimensional simulations of the impact of southern-ocean nutrient depletion on atmospheric CO_2 and ocean chemistry. *Limnology & Oceanography*, *36*(8), 1928–1950. https://doi.org/10.4319/lo.1991.36.8.1928

Smetacek, V., & Naqvi, S. W. (2008). The next generation of iron fertilization experiments in the southern ocean. *Philosophical Transactions of the Royal Society A: Mathematical, Physical & Engineering Sciences*, *366*(1882), 3947–3967. https://doi.org/10.1098/rsta.2008.0144

Street, J. H., & Paytan, A. (2005). Iron, phytoplankton growth, and the carbon cycle. *Biogeochemical Cycles of Elements*, *43*, 153–193.

Strong, A. L., Cullen, J., & Chisholm, S. (2009). Ocean fertilization science, policy, and commerce. *Oceanography*, *22*(3), 236–261. https://doi.org/10.5670/oceanog.2009.83

Tian, H., Chen, G., Lu, C., Xu, X., Ren, W., Zhang, B., et al. (2017). Global methane and nitrous oxide emissions from terrestrial ecosystems due to multiple environmental changes. *Ecosystem Health and Sustainability*, *1*(1), 1–20. https://doi.org/10.1890/ehs14-0015.1

Wang, W. L., Moore, J. K., Martiny, A. C., & Primeau, F. W. (2019). Convergent estimates of marine nitrogen fixation. *Nature*, *566*(7743), 205–211. https://doi.org/10.1038/s41586-019-0911-2

Watson, A. J., Bakker, D. C. E., Ridgwell, A. J., Boyd, P. W., & Law, C. S. (2000). Effect of iron supply on southern ocean CO_2 uptake and implications for glacial atmospheric CO_2. *Nature*, *407*(6805), 730–733. https://doi.org/10.1038/35037561

Yoon, J. E., Yoo, K.-C., Macdonald, A. M., Yoon, H.-I., Park, K.-T., Yang, E. J., et al. (2018). Reviews and syntheses: Ocean iron fertilization experiments—Past, present, and future looking to a future Korean Iron Fertilization experiment in the southern ocean (KIFES) project. *Biogeosciences*, *15*(19), 5847–5889. https://doi.org/10.5194/bg-15-5847-2018